Explaining the Opacity of the Solar Continuum at Visible and Infrared Wavelengths

Håkon Fossheim

https://github.com/fosheimdet/AST4310/tree/master/SSB

Institute of Theoretical Astrophysics, P.O. Box 1029, Blindern, N–0315 Oslo, Norway

Abstract. The solar continuum at visible and infrared wavelengths have been studied using data from Fontenla *et al*. (1993) and Allen (1973). This was done under the assumption that the solar atmosphere is horizontally homogeneous and in hydrostatic equilibrium. A correlation between brightness temperature and transmittance was found. The Sun's atmosphere was found to be more opaque to visible and near infrared light than Earth, mainly due to H⁻ extinction. The local thermodynamical equilibrium Eddington-Barbier approximation was found to hold reasonably well in the atmosphere. Furthermore, light with a wavelength of 1.6 μm was found to form deepest in the solar atmosphere.

1. Introduction

The large opacity of the Sun in the visible and infrared wavelengths compared to that of Earth's atmosphere was in the first decades of the twentieth century an unsolved mystery on par with the quest for finding the subatomic energy source of the Sun. A comparison between the column mass density and the particle density at the base of Earth's atmosphere and the height at which the solar gas becomes opaque, namely $\tau = 1$, will be made, showing that the sunlight passes through a far larger column mass in the Earth's atmosphere then in the Solar atmosphere, even though the molecules in Earth's atmosphere are much larger the Hydrogen atoms and electrons making up the majority of the Sun's atmosphere.

In 1939, Wildt suggested that the source of this photospheric extinction might be due to H⁻ extinction, and in 1946 Chandrasekhar and Breen succeeded in showing that this was indeed the case.
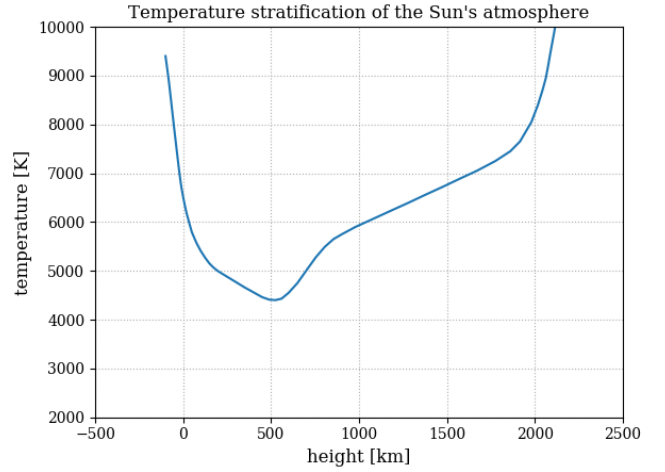
2. Theory and Results

2.1. Stratification of the solar atmosphere

The radial stratification of the solar atmosphere will now be studied using the FALC model, derived by Fontenla *et al*. (1993). This description of the solar photosphere and chromosphere was derived empirically, under the asumption that the solar atmosphere is horizontally homogeneous and in hydrostatic equilibrium.

Fig. 1: Temperature variation through the photosphere ($-100 \leq h \leq 525$km) and chromosphere ($525 \leq h \leq 2100$km).

Figure 1 shows the temperature variation through the Sun's atmosphere. Here $h = 0$ is defined as the height at which the optical depth at a wavelength of 500 nm is equal to one, $\tau_{500} = 1$.

Assuming hydrostatic equilibirium, the following equation holds

$$\frac{dP}{dr} = -\rho g \tag{1}$$

Integrating both sides gives

$$\int_{P(r=r_0)}^{P(r=\infty)} dP = -\int_{r_0}^{\infty} \rho g dr \tag{2}$$

Setting $P(r = \infty) = 0$ yields

$$-P_0 = -g \int_{r_0}^{\infty} \rho dr \tag{3}$$

Or

$$P_0 = gm \tag{4}$$

1

Where $m = \int_{r_0}^{\infty} \rho dr$ is defined as the column mass. From figure 2, the gravitational constant on the on the "Surface" was found to be $g_{surface} = 27392$ cm s^{-2}, which is in agreement with the actual value of $g_{\odot} = 274$ m s^{-2}
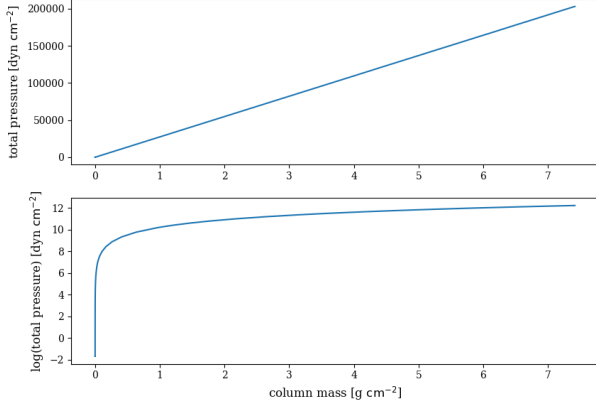

Fig. 2: Pressure plotted against column mass.

Figure 3 shows the mass density fraction of Hydrogen and Helium plotted against height. As seen, they are almost independent of height in the photosphere and chromosphere. The fraction of the total mass made up by the remaining elements (metals) was found to be $\approx 2.226 \cdot 10^{-3}$. The atmosphere of the sun thus consists of a bit more than 70% Hydrogen, a bit less than 30% Helium and about 0.2% metals.
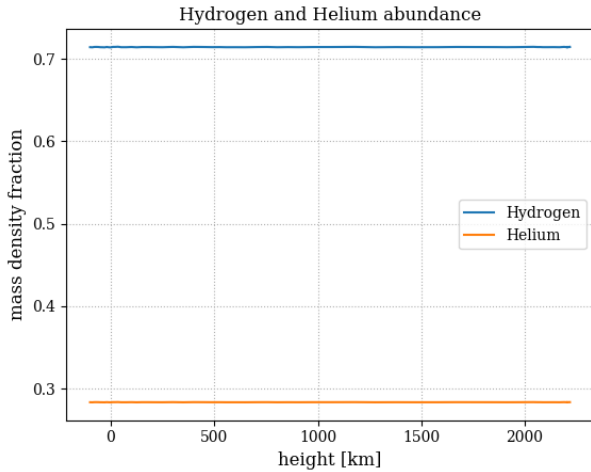

Fig. 3: Mass density fraction of Hydrogen and Helium plotted against height.

Figure 4 shows the column mass plotted against height. When the y-axis is made logarithmic, the curve becomes nearly straight. For an ideal gas in hydrostatic equilibrium, the density will decrease exponentially with height. The reason the lower panel of figure 4 deviates from a straight line might be because the Sun's atmosphere is not in hydrostatic equilibrium and/or is not a perfect ideal gas.
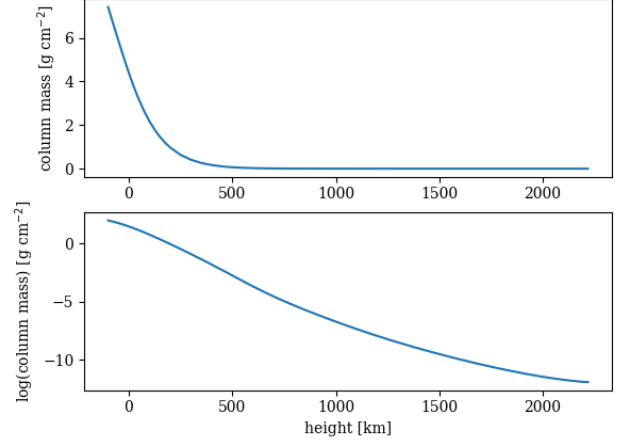

Fig. 4: Column mass against height.

For a gas in hydrostatic equilibrium the following holds

$$\rho(h) = \rho(0)e^{-h/H_\rho} \tag{5}$$

Where $H_\rho = \frac{k_b T}{Mg}$ for an ideal gas. Here k_b is the Boltzmann constant and M is the mean molecular weight. Using this expression with $M = m_H$ gives $H_{\rho_{ideal}} = 283.11$ km at $h = -100$ km. This is not realistic, as we have assumed that the atmosphere consists of only Hydrogen. Manipulating equation 5 and using the FALC data for the deep photosphere gives $H_{\rho_{exp}} = 147.1$ km. This estimate fits the data much better, as can be seen in figure 5.
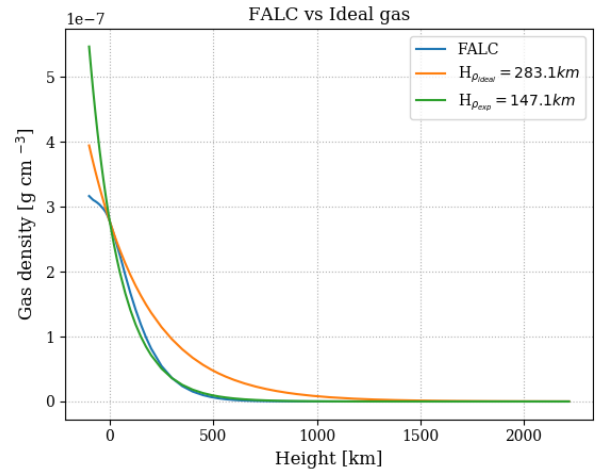

Fig. 5: Gas density against height.

Figure 6 shows the gas pressure given by FALC and the pressure found through the ideal gas law, using the Hydrogen and electron number densities plotted against height. As can be seen, $(n_H + n_e)kT$ matches the FALC pressure quite well at higher in the atmosphere, but starts to deviate at smaller heights. This deviation is plotted in figure 7.
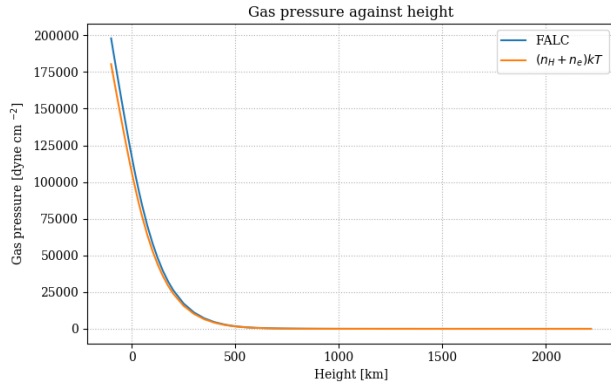
Fig. 6: Gas density against height. The blue curve represents the FALC data, while the orange curve is the pressure found through the ideal gas law, taking into account only the hydrogen and electron number densities.

Fig. 8:

As can be seen in figure 8, the proton density has a steep decline and reaches its minimum at $h \approx 500\,\mathrm{km}$. This is due to the steep drop-off observed in the temperature plot in figure 1. As the temperature decreases, there will be fewer and fewer H^+ atoms, i.e. protons. It is therefore no suprise that the proton density minimum coincides with the temperature minimum.

The figure also shows that the Hydrogen density and density of electrons not from Hydrogen, i.e. electrons from metals, are parallel over a considerable range. This implies that the metal abundance compared to Hydrogen is constant for low heights. As the temperature increases to 1500-2100 K in the outer chomosphere, the metals become more ionized, and the red curve therefore increases and is no longer parallel to the H^- curve.

As can be seen in figure 7, the pressure calculated using the ideal gas law deviates much less from the FALC pressure when the Helium number density is included.
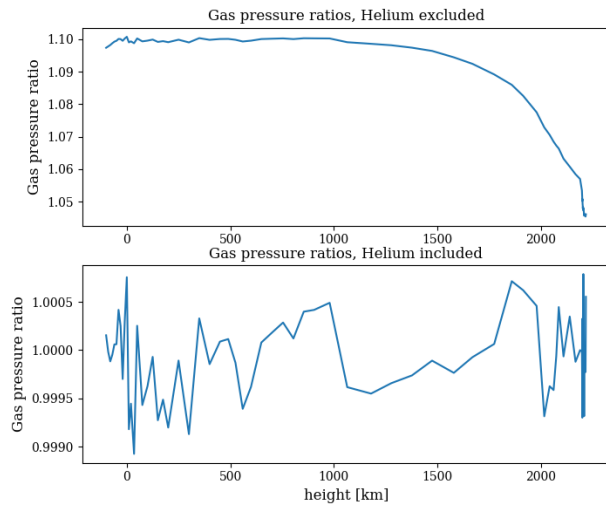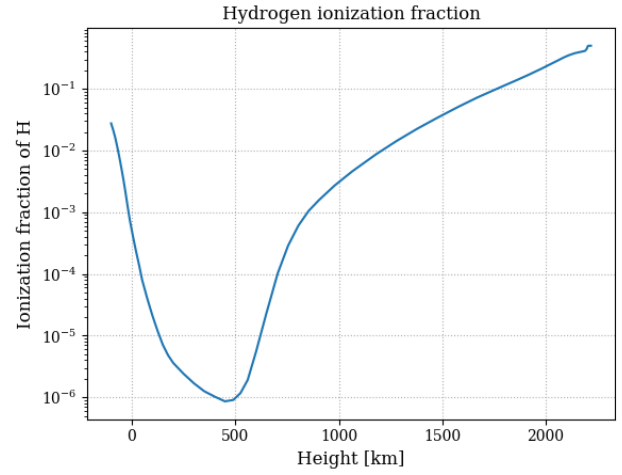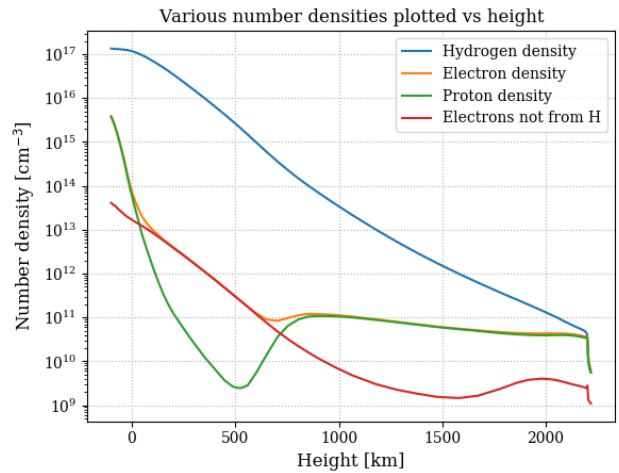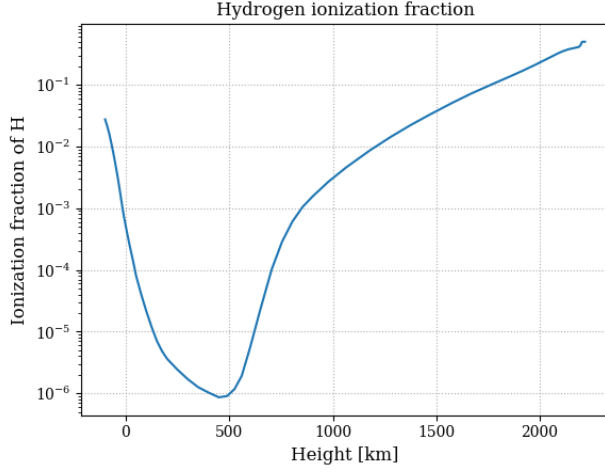

Fig. 7:

Fig. 9

Fig. 10: Hydrogen ionization fraction against height. As expected, this plot resembles that of the temperature plot due to the heavy temperature dependence of H^+.

Fig. 11: Temperature plotted against height.

In thermodynamical equilibrium, the photon density is given by

$$N_{phot} = \int_0^\infty \frac{u_\nu}{h\nu} d\nu \approx 20T^3 \qquad (6)$$

Where $u_\nu = \frac{du}{d\nu}$ is the derivative of the total energy density with respect to frequency, h is the Planck constant, ν is frequency and T is the temperature.

This approximation holds reasonably well in the photosphere where only visible radiation escapes. Here, the energy loss due to radiation is tiny in comparison with the local photospheric thermal contant. Higher up, TE will not hold due to the low density. Here the photon density is given by

Fig. 12: Pressure plotted against height.

$$N_{phot} \approx 20T_{eff}^3/2\pi \qquad (7)$$

Where $T_{eff} = 5770\,\text{K}$. At the deepest location in the FALC model, the hydrogen and photon densities are

$$N_{phot}(-100\,\text{km}) = 1.661 \cdot 10^{13}$$
$$n_{hyd}(-100\,\text{km}) = 1.351 \cdot 10^{17}$$

Giving the ratio $\frac{N_{phot}}{n_{hyd}} = 1.230 \cdot 10^{-4}$. At the highest location in the model, the densities are

$$N_{phot}(2218\,\text{km}) = 6.115 \cdot 10^{11}$$
$$n_{hyd}(2218\,\text{km}) = 5.575 \cdot 10^9$$

Giving $\frac{N_{phot}}{n_{hyd}} = 109.7$. The medium in the highest part of the model is insensitive to these photons due to the lack of collisions as a result of the low Hydrogen density.

2.2. Comparison with the Earth's atmosphere

This section repeats the some of the analysis for similar data on earth's atmosphere. This data is taken from Allen (1976).
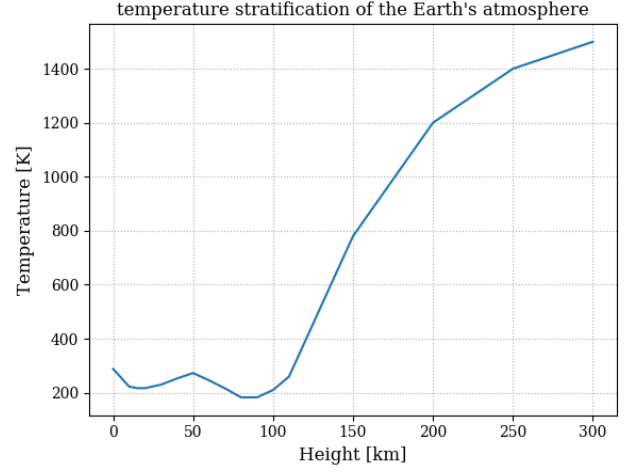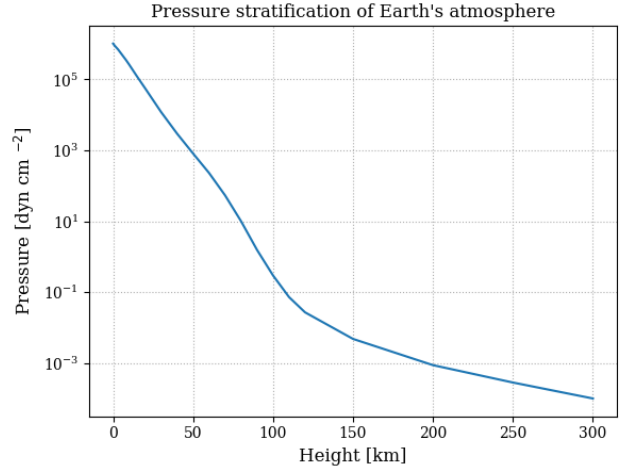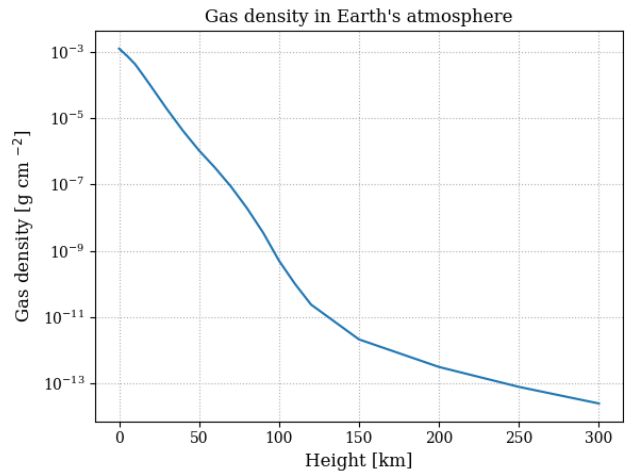

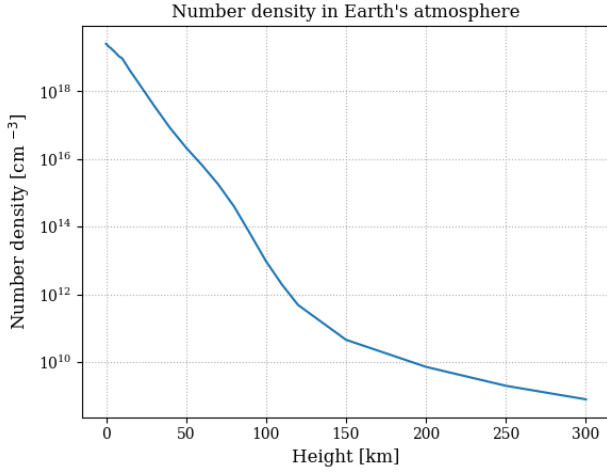Fig. 13: Gas density plotted against height.

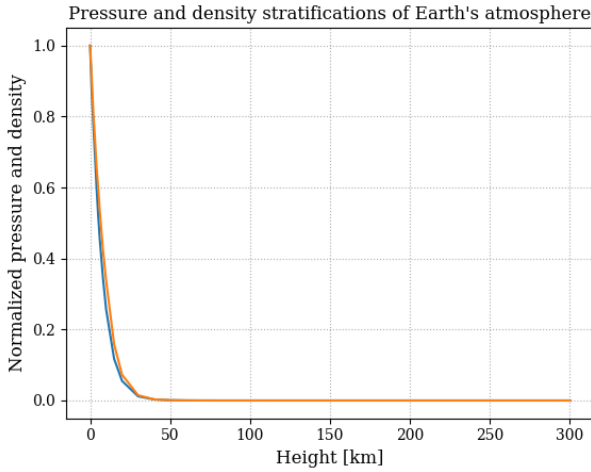Fig. 14: Number density plotted against height.

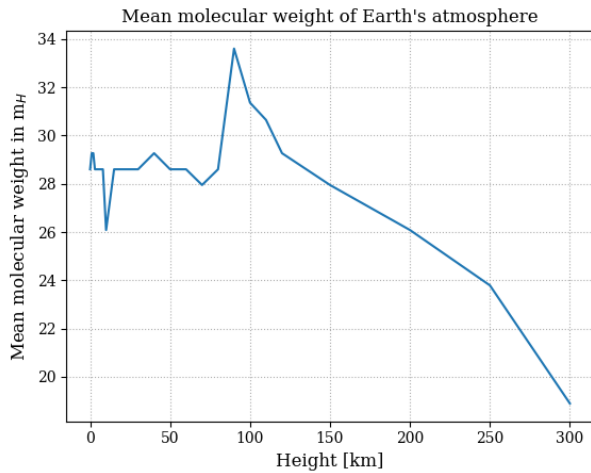Fig. 15: Normalized pressure and density plotted against height.

Fig. 16: Mean molecular weight plotted against height.

As can be seen in figure 16, the mean molecular weight μ_E decreases in the upper atmosphere. This is due to the fact that gases containing lighter elements rise due to their buoyancy and settle in the upper parts of the atmosphere, while gases consisting of heavier elements will flow downwards.

The density scale height can be estimated in the same way as the solar one. The scale height for the lower terrestrial atmosphere using the assumption of an ideal gas was found to be $H_{\rho_{ideal}} = 7.58$ km. Using the data given by Allen, it was found to be $H_{\rho_{exp}} = 9.79$ km. What makes this scale height differ from the solar one is mainly the temperature and surface gravity, but the mean molecular mass is also different.

Using $H_{\rho_{exp}} = 9.79$ km, the air pressure at the summit of Mount Everest, which lies at an altitude of 8848 m, is found to be 0.41 times that at sea level. The ratio of the particle densities at $h = 0$ in the two atmospheres was found to be

$$N_{earth}(h = 0) = 2.570 \cdot 10^{19}$$
$$N_{sun}(h = 0) = 1.300 \cdot 10^{17}$$

Giving $\frac{N_{earth}}{N_{sun}} = 197.6$ for the particle density ratio at the base of each atmosphere. Calculating the column mass at $h = 0$ for both atmospheres gives

$$m_{c_{earth}} = 1043.5 \text{ g}$$
$$m_{c_{sun}} = 4.4 \text{ g}$$

The sunshine photon density at earth is

$$N_{phot} = \pi \frac{R^2}{D^2} N_{phot}^{top} \tag{8}$$

With $N_{phot}^{top} = 6.115 \cdot 10^{11}$ cm^{-3} the photon density at the top of the FALC model, R the solar radius and D the sun-earth distance. Inserting for these values gives $N_{phot} = 4.155 \cdot 10^7$ cm^{-3}. The particle density and local thermal production in the air around us is

$$N_{part} = 2.570 \cdot 10^{19} \text{ cm}^{-3}$$
$$N_{phot_{thermal}} \approx 20T[h = 0]^3 = 4.778 \cdot 10^8 \text{ cm}^{-3}$$

These numbers tell shows that there are about 10 times as many photons created in the lowest part of earth's atmosphere as there are incoming photons.However, one has to take into account that the emitted by the earth have a longer wavelength, and therefore less energy.

3. Continuous spectrum from the solar atmosphere

The sun can be approximated as a Lambert radiator, and so the total flux through a surface element can be estimated by

$$\mathcal{F}_\nu = \mathcal{F}_\nu^+ - \mathcal{F}_\nu^- = \pi I_\nu \tag{9}$$

This can be averaged over the solar disc to get

$$\mathcal{F}_\nu = \pi F_\nu = \pi \langle I_\nu \rangle \tag{10}$$

Where F_ν is called the Astrophysical flux. F_ν and $\langle I_\nu \rangle$ therefore share the same units, namely that of intensity. In figure 17,

these quantities have been plotted. F_ν and I_ν are measured at the surface with spectral irregularities smoothed, while F'_ν and I'_ν measure the astrophysical flux and intensity at the solar surface for the continuum between lines, respectively.
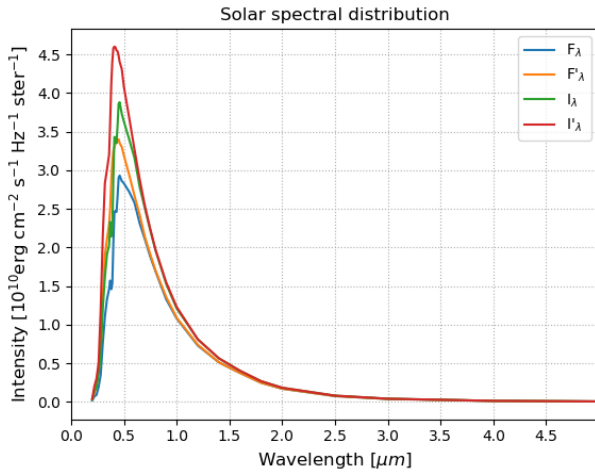

Fig. 17: Solar spectral distribution. Here F_λ, F'_λ, I_λ and I'_λ are plotted against wavelength.

The maximum value of I^c_ν was found to be $I^c_\nu = 4.6 \cdot 10^{10}$ cm^{-2} s^{-1} ster^{-1} μm^{-1} at $\lambda = 0.41$m.

These spectral distributions can be converted into values per frequency bandwidth $\Delta\nu = 1$ Hz. This is plotted in figure 18
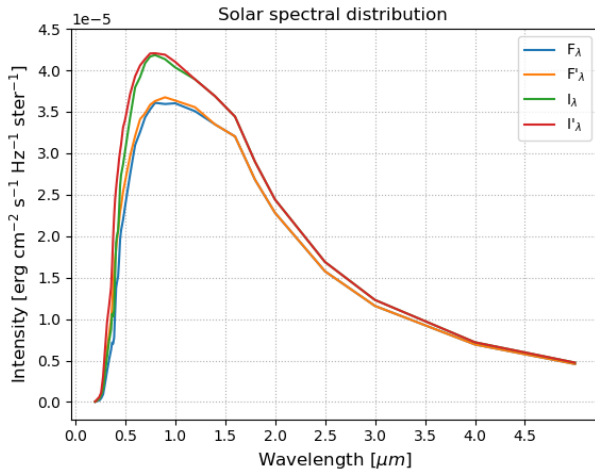

Fig. 18: Solar spectral distribution per frequency bandwidth $\Delta\nu = 1$ Hz.

If Payne's assumption is correct, then one would expect spectral lines to have the same shape as the population density when plotted against temperature.

The brightness temperature is the temperature required for the Planck function to have the same value as the observed intensity for a specific wavelength.

$$I_\lambda = B_\lambda(T_b) = \frac{2hc^2}{\lambda^5} \frac{1}{e^{hc/\lambda k_b T_b} - 1} \quad (11)$$

Inverting equation 11 to get the brightness temperature for a given intensity and wavelength gives

$$T_b = \frac{hc}{\lambda k_b \ln\left(\frac{2hc^2}{\lambda^5 I_\lambda} + 1\right)} \quad (12)$$

The brightness temperature as a function of wavelength is plotted in figure 19. As can be seen, the brightness temperature peaks at $\lambda \approx 1.6$ μm, which is in the near infrared. The plot of T_b reflects the opacity of the sun at different wavelengths, since the higher the temperature, the deeper in the sun's atmosphere the photons must originate. This is why figure 19 looks like the plot of the continuous extinction coefficient inverted, given by figure 5 in the assignment [**SSB**]
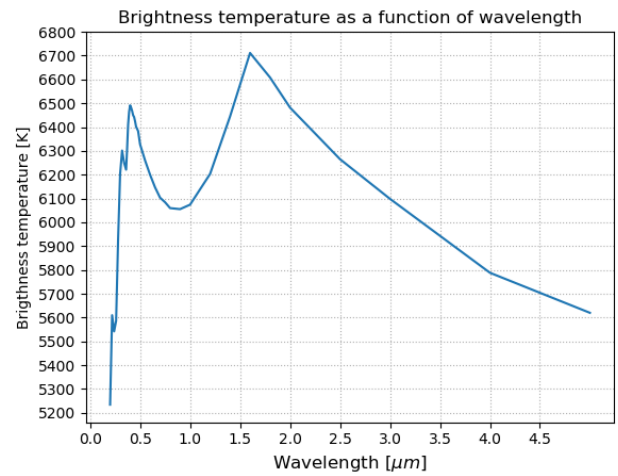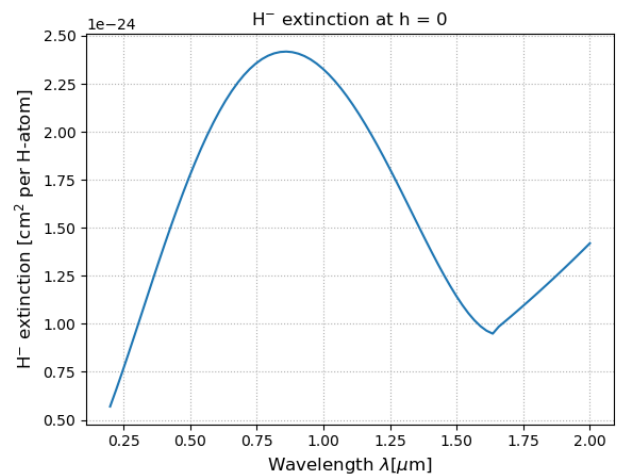

Fig. 19: Brightness temperature of the intensity taken from Allen plotted against wavelength.

3.1. Continuous extinction

The continuous extinction caused by H$^-$ is plotted against wavelength in figure 20 per Hydrogen atom. In figure 21 the inverse of the extinction, namely the transmittance is plotted.

Fig. 20: H$^-$ extinction plotted against wavelength at the surface.

6

As can be seen, the plot of the transmittance have a similar shape to that of the plot of brightness temperature.
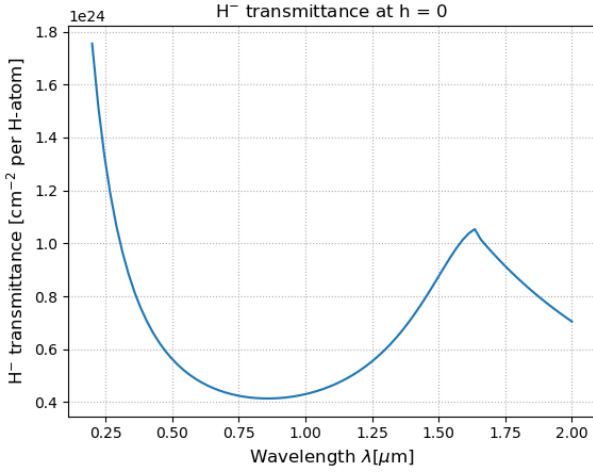

Fig. 21: H⁻ transmittance plotted against wavelength at the surface.

The H^{Minus} bound-free extinction differs strongly from the bound-free edges seen in HI where there is maximum extinction at the ionization limit and decay $\tilde{\lambda}^3$ for smaller wavelengths. This is due to the extra electron posessed by H⁻.

In figure 22, the extinction $\alpha_\lambda(\mathrm{H}^-)$ measured per cm path length is plotted against height. This plot needs to be logarithmic in the y-axis because the extinction is no longer measured pr. Hydrogen atom, but per cm path length. This will make $\alpha_\lambda(\mathrm{H}^-)$ vary greatly through the atmosphere due to the large differences in density.
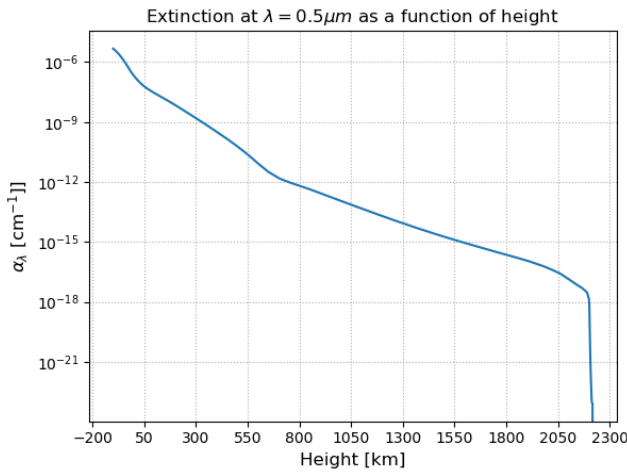

Fig. 22: Extinction measured per cm path plotted against height.

Next, let us include the extinction due to Thomson scattering. In order to do this, the Thomson cross-section per electron ($\sigma^T = 6.648 \cdot 10^{-25}$ cm²) is multiplied by the electron density. The result is shown in figure 23. As can be seen, the exctinction due to H⁻ dominates in the lower parts of the atmosphere, but declines steeply at around 2200 km. This is most likely due to the

steep temperature rise in this region, ionizing all the H⁻. For the higher parts of the atmosphere, Thomson exctinction dominates.
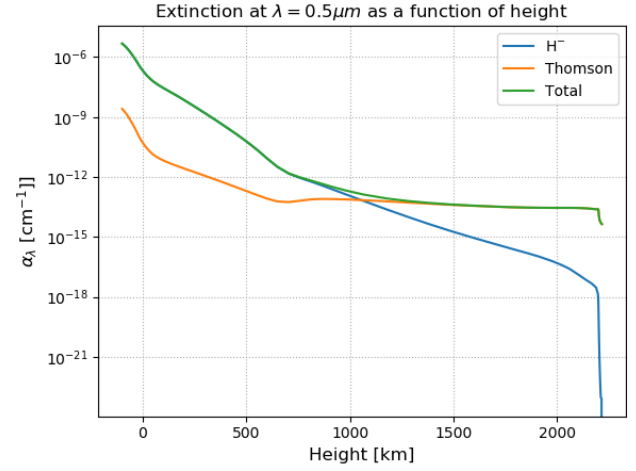

Fig. 23: Extinction measured per cm path plotted against height.

3.2. Optical depth

Now that the continuous extinction as a function of height is known, the corresponding optical depth can be calculated

$$\tau_\lambda(h_0) \equiv - \int_\infty^{h_0} \alpha_\lambda^c dh \qquad (13)$$

at any height h_0. This is done numerically using trapezoidal integration. The result is compared with the optical depth given by FALC in figure 24. As can be seen, the optical depth calculated using H⁻ and Thomson extinction matches very well with the data from FALC in the lower and higher parts of the atmosphere. The fit rather poor in the middle parts however.
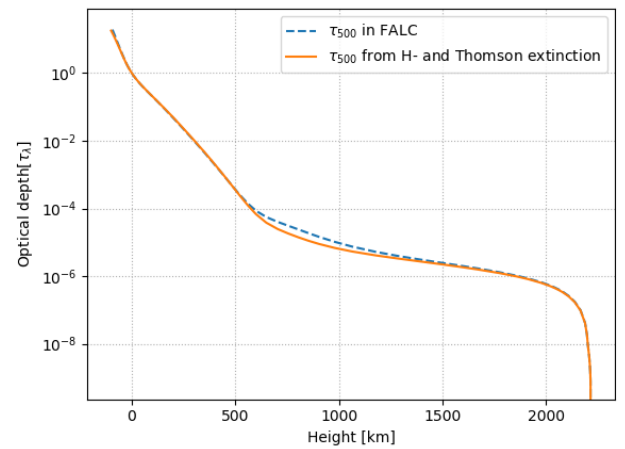

Fig. 24: Integrated optical depth at $\lambda = 500$ nm compared with the given optical depth in the FALC model.

3.3. Emergent intensity and height of formation

Assuming plane-parallel stratification, the intensity of radiation that emerges from the center of the solar disk is given by

$$I_\lambda = \int_0^\infty S_\lambda e^{-\tau_\lambda} d\tau_\lambda \tag{14}$$

The intensity distribution function

$$\frac{dI_\lambda}{dh} = S_\lambda e^{-\tau_\lambda} \alpha_\lambda \tag{15}$$

Shows the contribution of each layer to the emergent intensity. Its weighted mean defines the "mean height of formation":

$$\langle h \rangle \equiv \frac{\int_0^\infty h \left(\frac{dI_\lambda}{dh} \right) dh}{\int_0^\infty \left(\frac{dI_\lambda}{dh} \right) dh} = \frac{\int_0^\infty h S_\lambda e^{-\tau_\lambda} d\tau_\lambda}{\int_0^\infty S_\lambda e^{-\tau_\lambda} d\tau_\lambda} \tag{16}$$

The contribution along with the mean height of formation for $\lambda = 500$ nm is plotted in figure 25

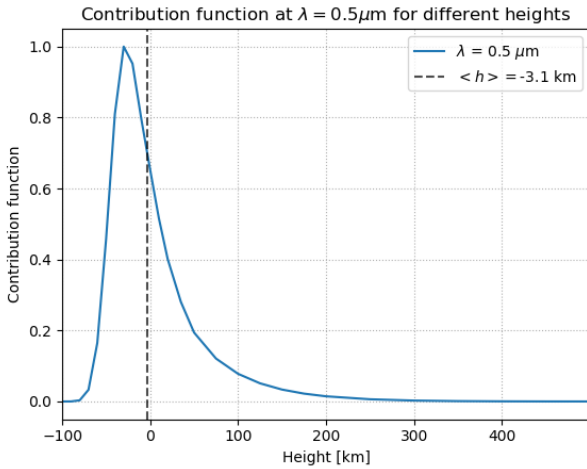Fig. 25: Contribution function plotted against height.

The computed intensity at $\lambda = 500$ nm was found to be $4.29 \cdot 10^{14}$ erg cm^{-2} s^{-1} ster^{-1} cm^{-1}, while the observed intensity at this wavelength is $4.08 \cdot 10^{14}$ erg cm^{-2} s^{-1} ster^{-1} cm^{-1}. The mean height of formation at $\lambda = 500$ nm is -3.138 km.

Figure 26 shows the peak normalized contribution function for different wavelengths. As seen, the light with wavelength $\lambda = 1.6\,\mu$m forms deepest in the atmosphere, in accordance with the plot for brightness temperature and the H$^-$ extinction. With the exception of $\lambda = 1.6$ the other wavelengths are formed consecutively higher in the atmosphere for longer wavelengths.
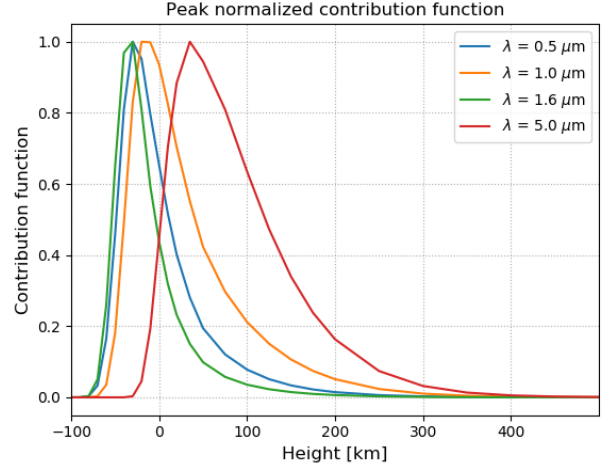

Fig. 26: Normalized contribution function for different wavelengths plotted against height.

Table 1 checks the validity of the LTE Eddington-Barbier approximation $I_\lambda \approx B_\lambda(T[\tau_\lambda = 1])$ by comparing the mean heights of formation with the $\tau_\lambda = 1$ locations and with the locations whete $T_b = T(h)$ for different wavelengths. As can be seen, these heights differ by a few kilometres, but this deviation is small compared to the height of the whole atmosphere. The LTE E-B can there be said to hold.

λ	$\langle h \rangle$ [km]	$h(\tau_\lambda = 1)$ [km]	$h(T = T_b)$ [km]
0.5 μm	-3.14	0.0	10
1.0 μm	24.1	10	20
1.6 μm	-17.9	-30	-20
5.0 μm	75.9	50	75

Table 1: Comparison of the mean heights of formation with the $\tau_\lambda = 1$ locations and with the locations whete $T_b = T(h)$ for different wavelengths.

3.4. Limb darkening

By repeating the integration in a loop over all the wavelengths given in solspect.dat, the emergent continuum is calculated as a function of wavelength. This is plotted against the observed continuum in figure 27. The deviation seen in this plot is mostly due to the fact that the metallicity of the solar atmosphere was not taken into account.
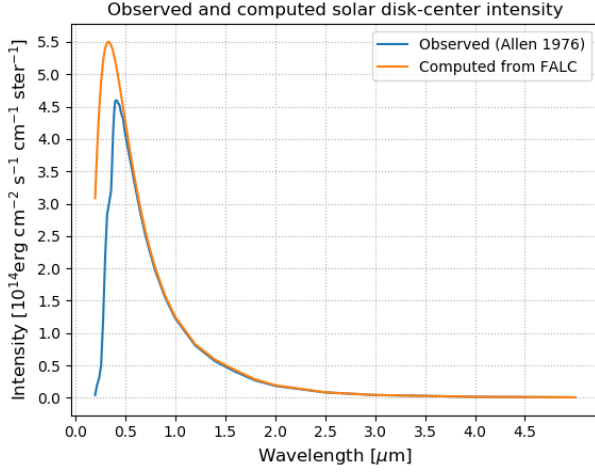
Fig. 27: Computed vs. observed solar disk-center intensity plotted against wavelength.

Fig. 29: Emergent intensity for different wavelengths plotted against μ.

3.5. Limb Darkening

The emergent intensity can be calculated for different viewing angles by slightly modifying equation 14.

$$I_\lambda(0, \mu) = \int_0^\infty S_\lambda e^{-\tau_\lambda/\mu} d\tau_\lambda/\mu \qquad (17)$$

Here $\mu = \cos\theta$ where θ is the angle between the observer and the normal to the solar surface. Repeating this intensity evaluation over an outer loop for different values of μ gives the plot in figure 28.

Fig. 30: Emergent intensity for different wavelengths plotted against $r/R_\odot$.

3.6. Flux integration

The emergent intensity can now be integrated over emergence angle to get the emergent astrophysical flux

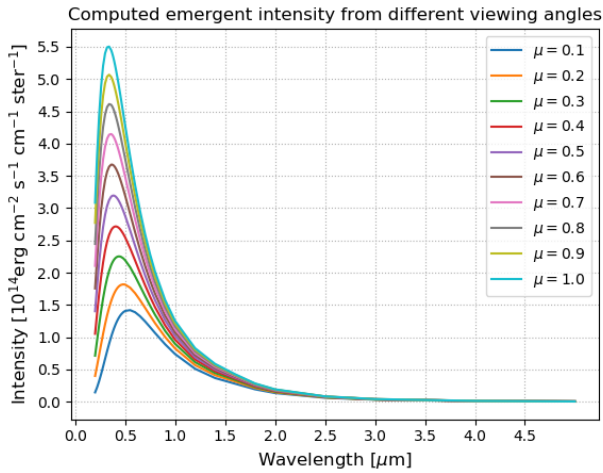$$F_\lambda(0) = 2 \int_0^1 I_\lambda(0, \mu)\mu d\mu \qquad (18)$$

Fig. 28: Emergent intensity for different viewing angles plotted against wavelength.

A plot of $I_\lambda(0, \mu)/I_\lambda(0, 1)$ against μ for a few selected wavelengths is seen in figure 29.
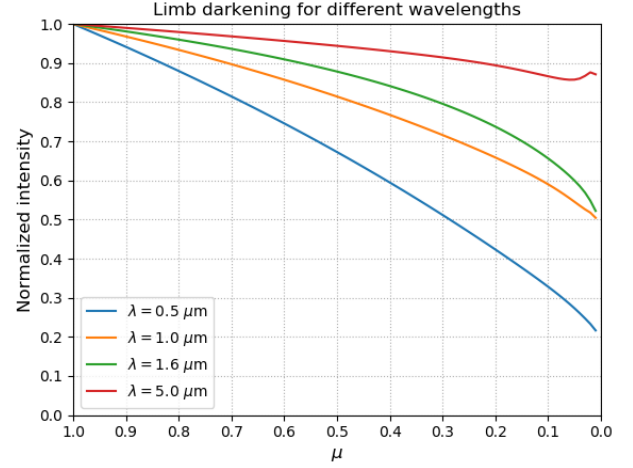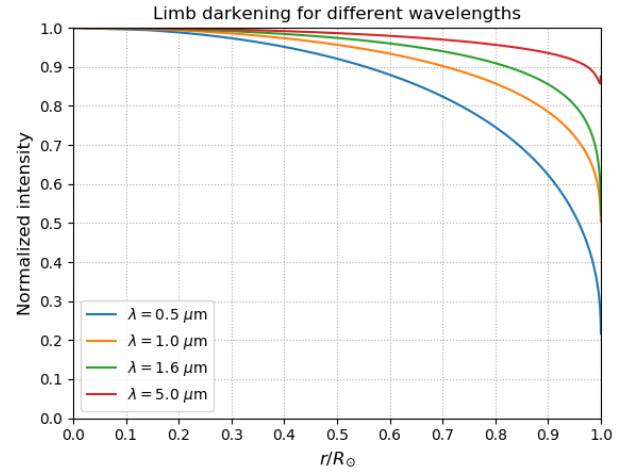
Because equation 17 can not be evaluated at $\mu = 0$, the integral is evaluated with open quadrature, neglecting the endpoints. Non-equidistant Gaussian quadrature was used, and the code use is given on the course website. The result is plotted in figure 30
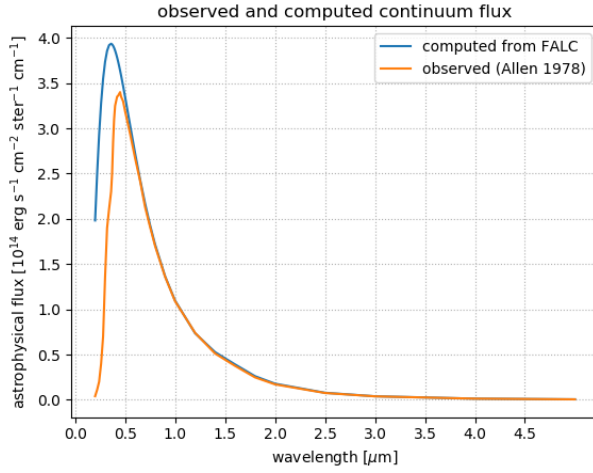
Fig. 31: Emergent solar flux compared to observed flux.

.

4. Discussion

The assumption of that the solar atmosphere is horizontally homogeneous, i.e. made of plane parallel layers does not hold, as the Sun is a sphere. Neither does the assumption of hydrostatic equilibrium (time independent) hold since the Sun's atmosphere is constantly evolving. The metallicity of the Sun was ignored for example when computing the disk-center intensity, which lead to deviation from the observed value.

The photon production at a height of $h = 0$ in the Earth's atmosphere was found to be an order of magnitude higher than that received from the Sun. What wasn't taken into account was the wavelength of the created photons. These are larger than the wavelength of the incoming photons, and so performing a calculation of the energy balance would likely show that the emitted energy is less than the incoming energy.

5. Conclusion

A comparison of temperature, gas density and number density was made between the solar atmosphere and the terrestrial atmosphere. At the base of Earth's atmosphere, both the number density and column mass was found to be greater. Also the local thermal photon production at the base of Earth's atmosphere was found to be an order of magnitude higher than that produced by the Sun at visible and infrared wavelengths. Light with the wavelength of 1.6μm was found to form deepest in the solar atmosphere. The LTE Eddington-Barbier approximation was found to hold reasonably well, and the Sun was found to have a limb darkening due to lower temperatures in the upper atmosphere.

References

SSBR.J. Rutten. Stellar Spectra B, LTE Line Formation. August 14, 2010 FontenlaFontenla, J.M., Avrett, E.H., and Loeser, R.: 1993, Astrophys. J. 406, 319 AllenAllen, C.W.: 1976, Astrophysical Quantities, Athlone Press, Univ. London